

1 **A deep learning classification task for accurate brain navigation during** 2 **functional ultrasound imaging**

3

4 **Authorship**

5 Théo Lambert^{1,2,3,4}, Clément Brunner^{1,2,3,4}, Dries Kil^{1,2,3,4}, Roel Wuyts³, Ellie D'Hondt³ &
6 Alan Urban^{1,2,3,4,*}

7

8 **Affiliations**

9 ¹ Neuro-Electronics Research Flanders, Leuven, Belgium

10 ² VIB, Leuven, Belgium

11 ³ Imec, Leuven, Belgium

12 ⁴ Department of Neuroscience, Faculty of Medicine, KU Leuven, Leuven, Belgium

13

14 * Corresponding author.

15 E-mail address: alan.urban@nerf.be

16

17 **Abstract**

18 Functional ultrasound imaging is a breakthrough technology for imaging brain activity at
19 high spatiotemporal resolution. As it monitors hemodynamic activity, the resulting images
20 are a non-standard representation of local anatomy. This leads to difficulties when
21 determining the exact anatomical location of the recorded image, which is necessary for
22 correctly interpreting the data. Here we propose a convolutional neural network-based
23 framework for accurately navigating the brain during functional ultrasound imaging solely
24 based on vascular landmarks. Our approach uses an image classification task to identify
25 a suitable set of reference positions, from which the anatomical position of an image can
26 be inferred with a precision of $102 \pm 98 \mu\text{m}$. Further analysis revealed that the predictions
27 are driven by deep brain areas. The robustness of our approach was validated using an
28 ischemic stroke model. It confirms that functional ultrasound imaging information is
29 sufficient for positioning even when local blood flow is disrupted, as observed in many
30 brain pathologies.

31 Introduction

32 The brain is often identified as the most complex organ of the human body. It consists of
33 very intricate webs of interconnected neurons and is responsible for every thought, action,
34 memory and feeling that we experience. To support their activity, neurons require a large
35 amount oxygen and nutrients, which is dynamically provided by a complex vascular
36 system¹⁻³.

37
38 As neurons do not have internal reserves of energy, their firing creates an energy
39 demand, which causes a local increase in blood flow^{4,5}. This mechanism linking neuronal
40 firing to a local increase in cerebral blood flow is also known as neurovascular coupling^{6,7}.
41 Monitoring these local hemodynamic changes forms the basis of several functional brain
42 imaging techniques⁸. The leading technology is blood-oxygen-level-dependent functional
43 magnetic resonance imaging (BOLD-fMRI)⁹, which is widely used in clinical studies¹⁰.
44 However, in a preclinical context, the spatiotemporal resolution of this technique is limited
45 and the required infrastructure make it expensive while implementing complex behavioral
46 paradigms is challenging^{8,11}.

47
48 Overcoming these limitations, functional ultrasound imaging (fUSI) is a breakthrough
49 technology combining large depth of field, high spatiotemporal resolution and
50 affordability^{8,12}. fUSI tracks hemodynamic changes in small vessels at several frames per
51 second using ultrafast plane-wave illumination of the tissue¹³⁻¹⁵. Similar to BOLD-fMRI,
52 the fluctuations in cerebral blood volume which are measured with fUSI are a proxy of
53 local neuronal activity¹⁶⁻¹⁹. In particular, fUSI has recently been used in preclinical
54 research to identify the brain regions involved in the optokinetic reflex¹⁷, to map the
55 networks activated by specific cell types in the superior colliculus¹⁸ and to report functional
56 activity in primates during active tasks and visual stimulation^{20,21}.

57
58 A peculiarity of the technology is that, unlike fMRI, a fUSI recording only provides
59 information on the local vasculature - termed a micro-Doppler image - which is a non-
60 standard anatomical representation. Navigating the brain using this information has
61 proven to be challenging and requires expert knowledge of the vasculature. Indeed, for
62 interpreting the recorded activity, scientists need to be able to map the hemodynamic
63 changes to the corresponding anatomical regions. This is typically performed by
64 registering the data to a reference atlas such as the Allen Brain²² or Paxinos atlas²³. To
65 achieve such registration, it is necessary to identify the anatomical position at which the
66 data is acquired precisely. This is usually done by looking for morphological similarities
67 between the recorded image and the anatomical reference atlas, e.g., cortical thickness
68 or anatomical structures such as the ventricles and vascular landmarks. This topic has
69 been recently addressed in ref.²⁴, who developed an automated ultrasound-based neuro-
70 navigation system to roughly identify their position in the brain. In their approach, they
71 couple online registration of the recorded micro-Doppler volume to a pre-registered
72 reference volume acquired at the start of every experiment.

73
74 Here we propose an alternative deep learning approach leveraging the power of
75 Convolutional Neural Networks (CNN) for image classification. Solely based on the
76 vasculature, it allows for accurately locating single micro-Doppler images without the
77 need for a pre-registered reference. Instead of predicting real-valued positions by
78 registering the recorded micro-Doppler image to a vascular template, we defined multiple
79 target classes, each corresponding to an anatomical position. This set of key positions
80 forms a reference grid on the brain from which one can infer the actual location of the
81 recorded image.

82 We selected a DenseNet121-CNN and an additive chi-square kernel support vector
83 machine with a histogram of oriented gradients features extractor (HOG-SVM)
84 respectively as main and baseline models^{25,26}, based on a prior performance evaluation.
85 Both were trained for classification on high-quality micro-Doppler images from *in vivo*
86 acquisitions on a set of 51 rats accounting for the intrinsic morphological variability
87 encountered in brain-wide navigation. First, we compared the two models in terms of
88 effect of the spacing between consecutive classes on the classification accuracy. The
89 spacing with the highest classification accuracy allowed us to identify a suitable set of key
90 anatomical positions. Second, we calculated the expected resolution we can achieve
91 based on these key positions. Third, we used the Gradient-weighted Class Activation Map
92 (GradCAM) technique to locate the discriminative features underlying accurate
93 classification²⁷. Finally, the robustness of the model was evaluated in a rat stroke model
94 where the cerebral blood flow is locally disrupted. Our approach has shown to be robust
95 to such image degradation, with a very limited effect on the quality of the predictions.
96

97 Results

98 **Micro-Doppler datasets.** The work presented here was performed using a micro-
99 Doppler dataset that was acquired from 51 rats. By stepping the ultrasound probe along
100 the antero-posterior axis of the brain, images were acquired in different coronal planes,
101 with an in-plane resolution of 100×110 μm and 300 μm slice thickness. The step size
102 between consecutive images was set at 125 μm (Fig. 1a) from the anatomical reference
103 point Bregma (B) +3.0 to -6.5 mm. Fig. 1.b displays example micro-Doppler images, on
104 which major anatomical structures were annotated.
105

106 **Anatomical reference grid: optimal spacing of key positions based on their**
107 **classification accuracy.** To determine which set of key positions is the most suited for
108 forming a reference grid, five datasets were created by down-sampling the initial brain
109 scans from the original step size (125 μm) to step values ranging from 250 to 750 μm
110 (Fig. 1c). Each dataset can be identified by its step size subscripted with the
111 corresponding number of positions, e.g., '500₂₀' stands for the dataset with a 500 μm step
112 size therefore comprising 20 images per animal. This dataset is depicted in
113 Supplementary Fig. 1, with major vessels labeled using a vascular atlas²⁸.
114

115 After a preliminary performance evaluation (Supplementary Table 1, Materials and
116 Methods – Model selection), a DenseNet121-CNN and HOG-SVM with additive chi-
117 square kernel were selected respectively as main and baseline models^{21,22}. Both were
118 trained to classify images with respect to their anatomical position on a subset of 25 rats.
119 The hyperparameters were tuned on a validation set of 13 rats, and their performance
120 were assessed on a testing set of 13 animals.
121

122 For both models, we observed an increase in the classification accuracy along with the
123 step size, ranging from respectively 56.2% / 58% (dataset 250₃₉) to respectively 98.2% /
124 95.9% (dataset 750₁₃), for DenseNet121-CNN and HOG-SVM (Fig. 1d, Supplementary
125 Table 2). The validation and testing accuracies are broadly similar, and interestingly, the
126 largest drop in performance as compared to the previous dataset occurs for dataset 250₃₉
127 (-25.7% for DenseNet121 and -22.4% for HOG-SVM, Supplementary Table 2). This is
128 the only dataset whose step size is below the technology resolution, i.e., 300 μm.
129

130 The testing accuracy is lower for the HOG-SVM compared to the DenseNet121-CNN,
131 irrespective of the step size. However, the performance comparison using the McNemar²⁹
132 statistical test exhibited no statistically significant differences apart from dataset 500₂₀

133 (** $p=0.0012$, Supplementary Table 2). With regards to the extrema, both models achieve
 134 similar maximum class accuracy, while the DenseNet121-CNN provides respectively
 135 higher and lower minimum class accuracy than the HOG-SVM for datasets 625₁₅ / 500₂₀
 136 and 375₂₆ / 250₃₉. We selected dataset 500₂₀ as the set of key positions as the 500 μ m
 137 step size offers a good trade-off between the number of positions (20) and their
 138 identification confidence (DenseNet121-CNN: 93.1%; HOG-SVM: 85.0%).
 139

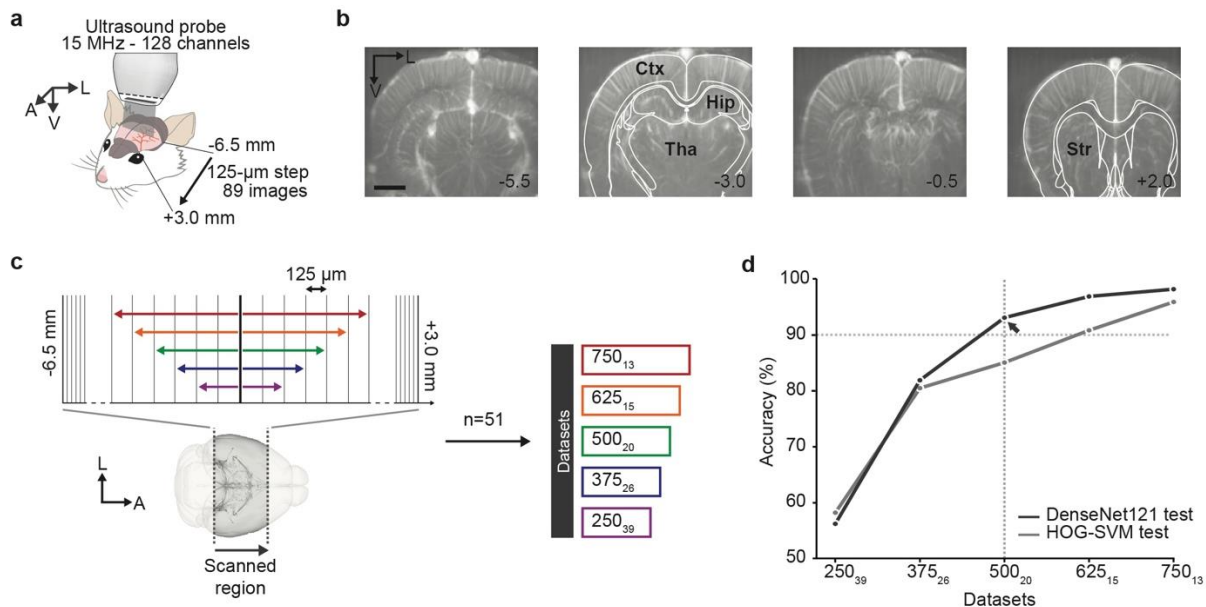


Fig. 1 Selection of the key positions based on classification accuracy. **a**, Schematic representation of the setup used for micro-Doppler imaging on rats. The ultrasonic probe was positioned along the antero-posterior axis using a motorized linear stage. The imaging was performed from B +4.0 to -7 mm with a 125 μ m step size for a total number of 89 images. A: anterior, L: left, V: ventral. **b**, Example micro-Doppler images extracted from a single rat. A simplified version of the Paxinos brain atlas²³ is overlaid in white. Large anatomical structures are identified in black. The number in lower right corner corresponds to the Bregma position (mm) of the image. Ctx: cortex, Hip: hippocampus, Tha: thalamus, Str: striatum. Scale bar: 2 mm. **c**, Schematic representation of the datasets created for determining the best set of key positions. Left: each set of 2D scans is down-sampled with 5 different factors, corresponding to the increase in the step size between two consecutive images, illustrated with colored arrows. Right: Each dataset can be identified by its step size subscripted with the corresponding number of positions (\langle spatial step \rangle number of locations). Arrows color code: purple 250 μ m, blue 375 μ m, green 500 μ m, orange 625 μ m, red 750 μ m. **d**, Testing classification accuracy of DenseNet121 and HOG-SVM models for each set of 2D scans ordered by their corresponding step size ($n=13$). The first set with accuracy above 90% is 500₂₀.

140
 141 **Resolution assessment.** We further investigated the per-Bregma position classification
 142 accuracies (Fig. 2a, Supplementary Table 3), which are non-uniformly distributed and
 143 range from 80 to 100%. The DenseNet121-CNN outperforms the HOG-SVM at every
 144 position, and the anterior part of the brain exhibits in general lower accuracies for both.
 145 The DenseNet121-CNN-associated confusion matrix reveals that misclassifications map
 146 to neighboring classes (Fig. 2b) and were not concentrated in a subset of animals.
 147

148 Based on this observation, we evaluated the actual resolution of our methodology. For
 149 each position, we created an additional dataset comprising of the position itself and
 150 images from the four closest anterior and posterior planes. The interval between those
 151 neighboring planes is 125 μ m, which is the smallest step size available from the original
 152 scan. For instance, the dataset for the position B +1.0 mm consists of positions +0.500,
 153 +0.625, +0.750, +0.875, +1.000, +1.125, +1.250, +1.375, +1.500 mm. All data from the
 154 validation and test sets were aggregated together.

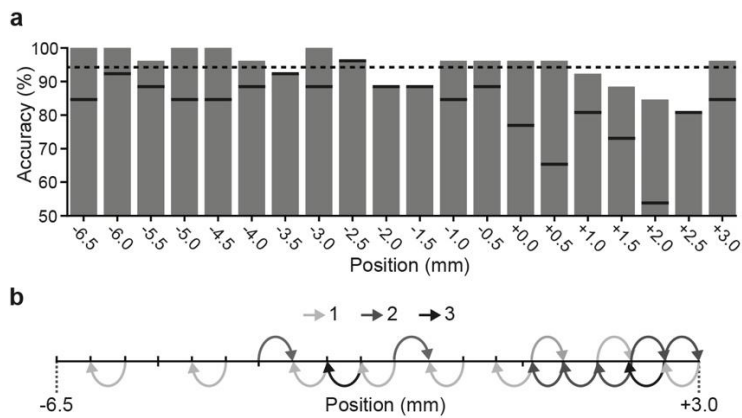


Fig. 2 Per-key position analysis of the DenseNet121 and HOG-SVM prediction. **a**, Per-Bregma position display of the DenseNet121 model accuracies for the dataset 500₂₀ evaluated on 26 animals, including validation and testing sets. The horizontal dashed line represents the mean classification accuracies of DenseNet121. For each position, the black bar represents the HOG-SVM model accuracy. **b**, Graphical representation of the DenseNet121 misclassifications. Each arrow goes from the true position to the predicted position. The light grey to black intensity represents the number of rats for which cross-sections were misclassified.

155
156
157
158
159
160
161

We processed each position with the DenseNet121-CNN model trained on the dataset 500₂₀ and collected the output probabilities. Then we identified the position with the highest probability and computed its absolute deviation from the target position. The mean and standard deviation of this absolute deviation are presented position-wise in Table 1.

Bregma position (mm)	Mean (µm)	Standard deviation (µm)
-6.5	NA	NA
-6.0	135	104
-5.5	87	103
-5.0	87	76
-4.5	77	78
-4.0	96	111
-3.5	48	78
-3.0	77	61
-2.5	87	76
-2.0	87	58
-1.5	77	78
-1.0	115	115
-0.5	135	77
0.0	135	77
0.5	115	104
1.0	106	96
1.5	115	104
2.0	106	108
2.5	163	142
3.0	NA	NA
Average	102	98

Table 1. Absolute deviation from the target position at each key position. Mean and standard deviation of the absolute deviation from the target position. For a given key position T, such absolute deviation corresponds to the positioning error made when taking the maximum probability of class T in a set comprising the target position and the four closest anterior and posterior planes.

162

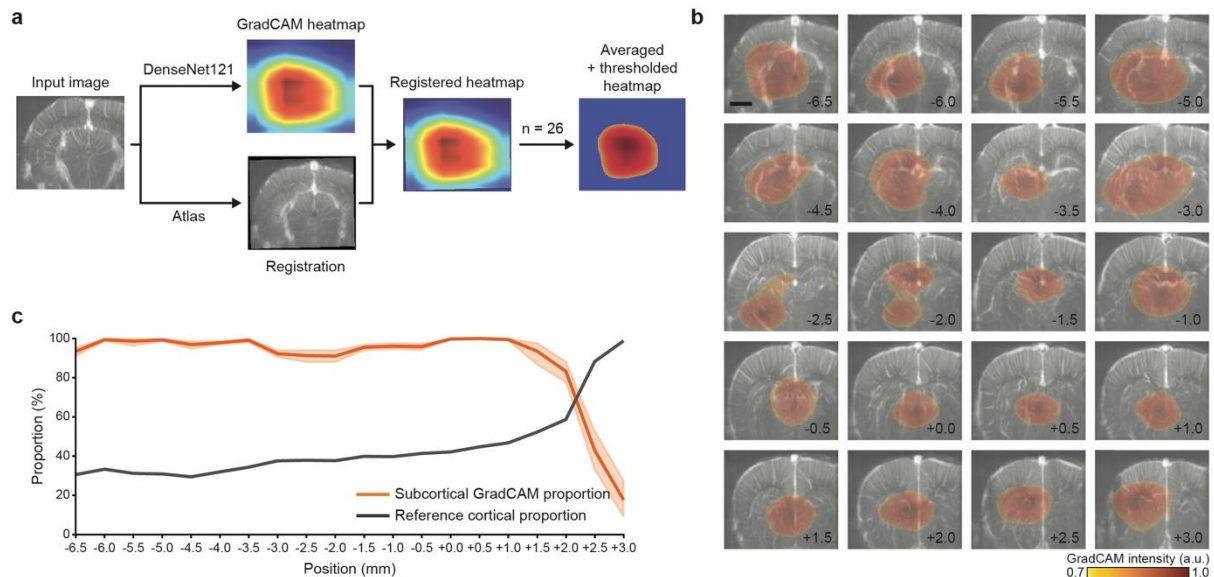
163 On average, the set of key positions in the dataset 500₂₀ are identified with a tolerance of
164 $102 \pm 98 \mu\text{m}$. Though the positions with highest deviations do not always correspond to
165 the lowest classification accuracy, most of the highest mean and standard deviation are
166 in the anterior part of the dataset.

167

168 **Spatial localization of the discriminative patterns.** To further estimate the reliability of
169 the key positions, we searched for the discriminative features using Gradient-weighted
170 Class Activation Maps (GradCAM)²⁷, a visualization technique that highlights the image
171 areas contributing the most to the network's inference toward a given prediction²⁷. We
172 registered the 2D scans with a digital version of the rat Paxinos atlas²³ to adjust for
173 potential differences in probe positioning and to allow for inter-animal comparison. For
174 each position, the GradCAM results were averaged across animals and thresholded to
175 alleviate the effect of interpolating these low resolution heatmaps (Fig. 3a).

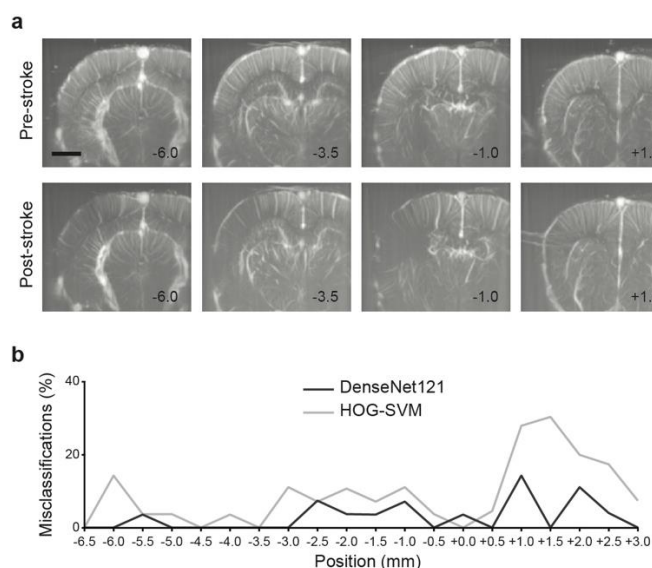
176

177 The averaged maps obtained for the set of keys positions were overlaid on the
178 corresponding set of registered micro-Doppler images (Fig. 3b). According to the
179 outcome, a single part in the image is driving the classification irrespective of the location
180 in the brain, at the exception of B -2.0 mm which exhibits two small, connected areas.
181 The identification of the local vasculature associated with the heat maps' location reveal
182 that the branches of several large vessels play a major role in the classification process
183 (Supplementary Fig. 1) including the thalamo-perforating arteries diverging from the
184 posterior cerebral artery (PCA), the thalamostriate veins and branches (tlv), and the
185 patterns produced by neighboring vessels such as the great cerebral vein of Galen and
186 the longitudinal hippocampal veins. Furthermore, we observed that the classification of
187 the four most anterior cross-sections (B +1.5, +2.0, +2.5, +3.0 mm) mostly relies on the
188 anterior cerebral artery (ACA), the azygos pericallosal arteries (APCA) and the
189 thalamostriate veins/arteries. Most of these vessels supply brain regions located in
190 subcortical regions, such as the thalamus, the hippocampus and the striatum as shown
191 in Fig. 1c.



192
193
194
195
196
197
198
199
200
201
202

Evaluating model robustness on a cortical stroke model. To further validate the reliability of subcortical vascular patterns for accurate position identification, we assessed the performance of both HOG-SVM and DenseNet121-CNN on a cortical stroke model. In these experiments, a subset of 28 rats were subjected to stroke by means of the permanent occlusion of the left middle cerebral artery provoking a significant decrease of signal (-60%) in the cortex of the left hemisphere. Whole-brain micro-Doppler scans were acquired before and 70 mins after stroke induction (Fig. 4a; see ref.³⁰ for details). From these 28 datasets, 14 were part of the training set, 7 of the validation set and 7 of the testing set.



203

204 To evaluate the accuracy of our models in such pathological conditions, the positions of
205 the post-stroke images were predicted with both DenseNet121-CNN and HOG-SVM
206 without prior re-training. For each model, the proportion of accurately classified pre-stroke
207 images whose position were incorrectly inferred after stroke was computed (Fig. 4b).
208 Images originally from the training, validation and testing sets were aggregated together
209 for this experiment as no substantial differences were observed. For the DenseNet121-
210 CNN model, the overall proportion of misclassification is 2.7%. Only two positions exhibit
211 a proportion higher than 10% (4/28 and 3/27 images respectively for B +1.0 and +2.0
212 mm) while for 75% of the positions only one image is misclassified. For the HOG-SVM
213 model, the overall proportion of misclassifications is 8.5%. 8 positions exhibit a proportion
214 higher than 10%, including 3 over 20%, and 45% of the positions have at most one
215 misclassified image. For both models we observed that the stroke has a larger effect on
216 the predictions in the anterior part of the brain (Fig. 4c).

217

218 Discussion

219 In this study, we proposed a novel framework for brain navigation in functional ultrasound
220 imaging experiments. Our approach relies on CNN-based image classification to identify
221 a set of anatomical positions that serve as a reference frame, from which the location of
222 a micro-Doppler image can be inferred with high precision. We selected a DenseNet121-
223 CNN as main model and an HOG-SVM as baseline model.

224

225 First, we defined a set of anatomical reference positions which act as the classes in our
226 image classification task. By analyzing the effect of different step sizes on the
227 classification accuracy we were able to select a set of key positions offering a trade-off
228 between the identification confidence and the number of positions in the reference grid.
229 We concluded that with a 500 μm step size, both models accurately classify each image
230 to the corresponding anatomical position (>90%). The effect of the step size on the
231 accuracy above 375 μm is linear-like for HOG-SVM while exponential-like for
232 DenseNet121. This can explain the statistically significant difference in performance on
233 datasets 500₂₀ and 625₁₅. Such decrease can be attributed to the similarity in vasculature
234 across neighboring planes at the technology resolution. This hypothesis is supported by
235 the drop in the minimum class accuracy along with the step size for both models. We then
236 computed on the set of key positions an estimated positioning error of $102 \pm 98 \mu\text{m}$ for
237 DenseNet121, which is smaller than the micro-Doppler image thickness (300 μm) and
238 therefore sufficient.

239

240 Further analysis using the GradCAM visualization technique revealed that the
241 classification was mainly driven by highly consistent vascular structures located in the
242 subcortex. This subcortical prevalence can partially be explained by the in-plane
243 resolution of the current fUSI technology: the voxel size of $100 \times 110 \times 300 \mu\text{m}^3$ is likely
244 insufficient to highlight the vascular differences between cortical areas, where the
245 penetrating arterioles have a diameter between 50 and 100 μm^1 . Another potential
246 explanation comes from the CNNs sensitivity to texture differences when pretrained on
247 ImageNet. This might explain why the cortical curvature and thickness variation across
248 anatomical locations are not decisive factors in our approach. Finally, we validated the
249 CNN's predictions in a rat stroke model where normal blood flow is disrupted. Analysis
250 revealed that the number of misclassified images was marginal compared to the pre-
251 stroke dataset (2% for DenseNet121-CNN, 8% for HOG-SVM), thus confirming the
252 robustness of the inference.

253

254 The automated positioning of micro-Doppler images is a problem that has only recently
255 been tackled. At the time of writing there is only one publication on this topic, where the
256 recorded micro-Doppler image is automatically registered to a pre-aligned reference
257 volume³¹. The main drawback of this method lies in the acquisition of a reference micro-
258 Doppler volume at the start of every experiment, which is manually registered to a brain
259 atlas. Our approach, on the other hand, does not require an animal-specific reference
260 and therefore offers more flexibility in the experimental design. Furthermore, due to the
261 large training dataset, our model is less sensitive to differences in brain size and shape,
262 including in pathological conditions such as stroke. This will be strengthened even further
263 as more fUSI data becomes available. Finally, the CNNs' computational efficiency allows
264 for real-time image identification and can therefore be seamlessly integrated in an
265 experimental workflow.

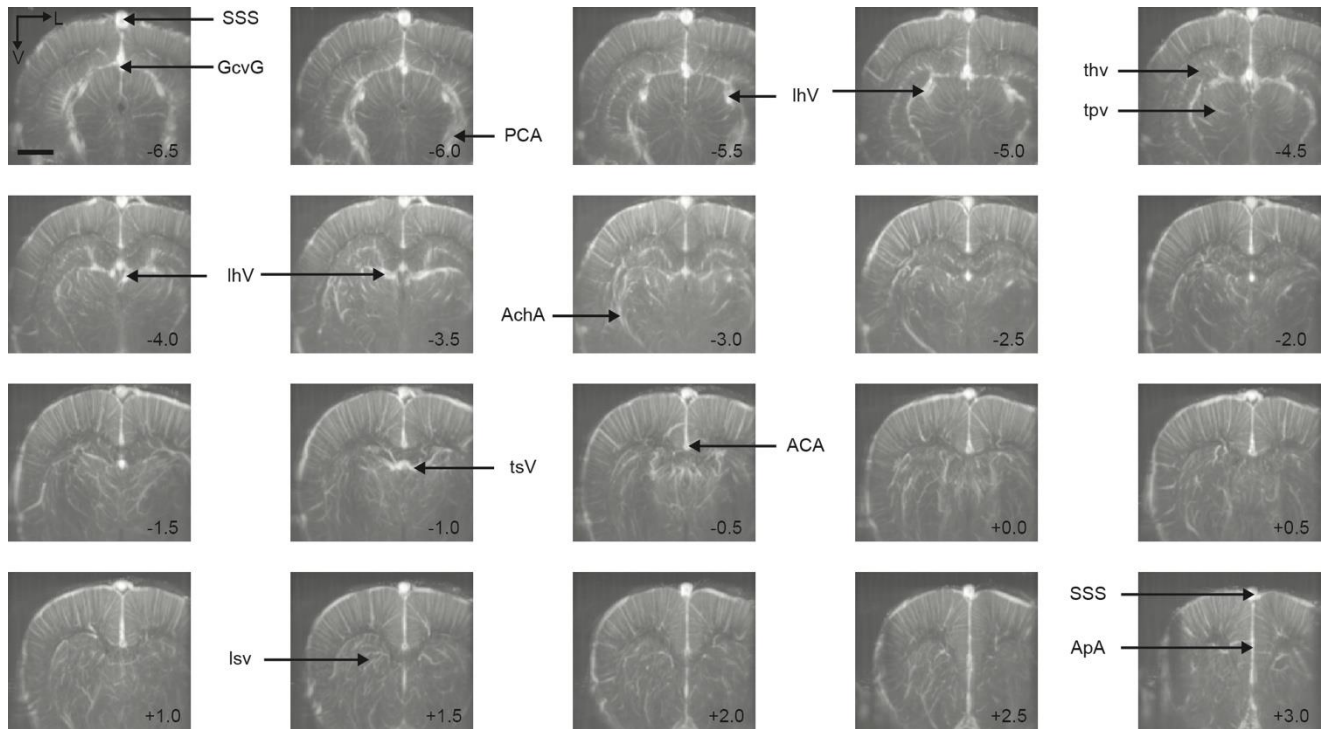
266
267 Although our work is validated on a rat model, we expect that the presented approach is
268 universal and can easily be adapted to different use cases, including applications in other
269 animal models such as non-human primates, pigeons or ferrets^{20,21,32,33}. Early results
270 support the applicability of our methodology to mice datasets (data not shown) and
271 elicited similar results. Future work should also focus on extending the model to different
272 probe orientations (e.g. sagittal) or different types of ultrasound transducers such as the
273 recently developed volumetric fUSI system^{34,35}, which acquires dozens of planes
274 simultaneously at the cost of a lower spatial resolution. Additionally, micro-Doppler
275 imaging has also been successfully applied to humans in neurosurgery³⁶⁻³⁸ and non-
276 invasively in newborns by imaging through the fontanel³⁹. In those contexts, an accurate
277 positioning methodology would be of great value but comes with new challenges, such
278 as the limited depth of imaging and the large differences in vessel scales. The increasing
279 adoption of fUSI and related data diversity will allow further generalization of this
280 approach.

281
282 To conclude, we believe that our methodology will constitute a valuable tool for the
283 neuroscientific community in the coming years, as it will allow non-expert users to exploit
284 the full potential of the fUSI technology.

285
286

287 **Supplementary Materials**

288



Supplementary Fig. 1, Set of micro-Doppler images extracted from the dataset 500₂₀ covering a large part of the brain for one rat. Major vessels are identified in black. Number corresponds to the Bregma position (mm) of the image. ACA: anterior cerebral artery, AchA: anterior choroidal artery, ApA: azygos pericallosal artery, GcvG: great cerebral vein of Galen, lhV: longitudinal hippocampal vein, lsv: lenticulostriate vessels, thv: transverse hippocampal vessels, tsV: thalamostriate vein, tpv: thalamoperforating vessels, SSS: superior sagittal sinus, Ctx: cortex, Hip: hippocampus, Tha: thalamus, Str: striatum, A: anterior, L: left, V: ventral. Scale bar: 2 mm.

289

290

Model	ResNet5 0	DenseNet12 1 (main)	HOG-SVM chi2 (baseline)	HOG-SVM rbf	SIFT-SVM rbf	PCA-SVM rbf
Validation accuracy (%)	82.5	85.2	71.6	65.1	29.3	53.5
Testing accuracy (%)	77.2	81.9	80.4	68.3	24.5	64.5

Supplementary Table 1. Performance evaluation of a set of classical models on dataset 375₂₆.

291

292

293

Step size (μm)		250	375	500	625	750
Number of positions		39	26	20	15	13
DenseNet121	Validation accuracy (%)	64.3	85.2	95.4	100	100
	Test accuracy (%)	56.2	81.9	93.1	96.9	98.2
	Difference between test and validation accuracy	8.1	3.3	2.3	3.1	1.8
	Maximum class accuracy test (%)	84.6	100	100	100	100
	Minimum class accuracy test (%)	0.0	30.8	84.6	84.6	84.6
HOG-SVM	Validation accuracy (%)	54	71.6	81.9	88.7	92.9
	Test accuracy (%)	58	80.4	85	90.8	95.9
	Difference between test and val. Accuracy	-4	-8.8	-3.1	-2.1	-3
	Maximum class accuracy (%)	84.6	100	100	100	100
	Minimum class accuracy (%)	20.3	61.5	53.8	53.8	84.6
McNemar test	Test statistic	86.00 0	28.00 0	12.00 0	4.000	1.000
	P-value	0.552	0.450	0.002 (**)	0.012 (*)	0.219

Supplementary Table 2. DenseNet121 and HOG-SVM performance metrics on the datasets with different step sizes. *p-value<0.05, **p-value<0.01.

294

295

Bregma position (mm)	-6.5	-6.0	-5.5	-5.0	-4.5	-4.0	-3.5	-3.0	-2.5	-2.0	-1.5	-1.0	-0.5	0.0	0.5	1.0	1.5	2.0	2.5	3.0
-----------------------------	------	------	------	------	------	------	------	------	------	------	------	------	------	-----	-----	-----	-----	-----	-----	-----

Validation set																					
Accuracy (%)	100	100	100	100	100	100	100	100	100	100	92.3	84.6	92.3	92.3	92.3	100	100	92.3	84.6	76.9	100
Precision	1.00	1.00	1.00	1.00	1.00	1.00	1.00	1.00	1.00	0.93	0.92	0.92	0.86	1.00	1.00	0.93	0.93	0.92	0.92	0.91	0.87
Recall	1.00	1.00	1.00	1.00	1.00	1.00	1.00	1.00	1.00	1.00	0.92	0.85	0.92	0.92	0.92	1.00	1.00	0.92	0.85	0.77	1.00
F1-score	1.00	1.00	1.00	1.00	1.00	1.00	1.00	1.00	1.00	0.96	0.92	0.88	0.89	0.96	0.96	0.96	0.96	0.92	0.88	0.83	0.93

Testing set																				
Accuracy (%)	100	100	92.3	100	100	92.3	84.6	100	92.3	84.6	92.3	100	100	100	92.3	84.6	84.6	84.6	84.6	92.3
Precision	1.00	0.93	1.00	1.00	0.93	1.00	1.00	0.81	0.86	1.00	1.00	0.93	1.00	0.93	0.86	0.92	0.92	0.79	0.85	1.00
Recall	1.00	1.00	0.92	1.00	1.00	0.92	0.85	1.00	0.92	0.85	0.92	1.00	1.00	1.00	0.92	0.85	0.85	0.85	0.85	0.92
F1-score	1.00	0.96	0.96	1.00	0.96	0.96	0.92	0.90	0.89	0.92	0.96	0.96	1.00	0.96	0.89	0.88	0.88	0.81	0.85	0.96

Supplementary Table 3. Per Bregma position classification metrics on dataset 500₂₀ of DenseNet121.

297 **Materials and Methods**

298 **Animals.** Experimental procedures were approved by the Committee on Animal Care of the Catholic University of
299 Leuven, in accordance with the national guidelines on the use of laboratory animals and the European Union
300 Directive for animal experiments (2010/63/EU). Adult male Sprague-Dawley rats (n=51; Janvier Labs, France) with
301 an initial weight between 200-300 g were housed in standard ventilated cages and kept in a 12:12 hrs reverse
302 dark/light cycle environment at a temperature of 22 °C with *ad libitum* access to food and water.

303
304 **Cranial window for brain-wide imaging and stroke induction.** A cranial window extended from B +4.0 to -7.0
305 mm AP, laterally ± 6.0 mm was performed in all rats under isoflurane anesthesia (Iso-Vet, Dechra, Belgium) with a
306 mixture of 5% isoflurane in compressed dry air was used to induce anesthesia, subsequently reduced to 2.0-2.5%
307 during surgery, and to 1.5% for imaging (see ref.³⁰ for details on surgical procedure). Xylocaine (0.5%, AstraZeneca,
308 England) and Metacam (0.2mg/kg, Boehringer Ingelheim, Canada) were injected subcutaneously as pre-operative
309 and post-operative analgesia; respectively. Intraperitoneal injection of 5% glucose solution was provided every 2hrs
310 to prevent dehydration. 28 rats were subjected to stroke by the mean of permanent occlusion of the distal branch
311 of the left middle cerebral artery as detailed in ref.³⁰.

312
313 **2D scan micro-Doppler ultrasound imaging of brain vasculature.** The data acquisition was performed using a
314 functional ultrasound imaging scanner equipped with custom acquisition and processing software described in
315 ref.¹¹. In short, the scanner is composed of a linear ultrasonic transducer (15 MHz, 128 elements, Xtech15, Vermon,
316 France) connected to 128-channel emission-reception electronics (Vantage, Verasonics, USA) that are both
317 controlled by a high-performance computing workstation (fUSI-2, AUTC, Estonia). The transducer was motorized
318 (T-LSM200A, Zaber Technologies Inc., Canada) to allow antero-posterior scanning of the brain. The acoustic
319 coupling between the brain and the probe is ensured by a 2 mm layer of ultrasound gel (Aquasonic Clear, Parker
320 Laboratories Inc, USA). Each coronal Doppler image is 12.8 mm width and 9 mm depth and is composed of 300
321 compound images acquired at 500 Hz. Each compound image is computed by adding nine plane-wave (4.5 kHz)
322 with angles from -12° to 12° with a 3° step. The blood signal was extracted from 300 compound images using a
323 single value decomposition filter and removing the 30 first singular vectors⁴⁰. The Doppler image is computed
324 as the mean intensity of the blood signal in these 300 frames that is an estimator of the cerebral blood volume^{14,15}.
325 This sequence enables a temporal resolution of 0.6 sec, an in-plane resolution of 100x110 μm , and an off-plane
326 (thickness of the image) of 300 μm ¹¹. Finally, we performed a high-resolution 2D scan of the brain vasculature
327 consisting of 89 coronal planes from B +4.0 to -7.0 mm spaced by 125 μm .

328
329 **Registration of micro-Doppler images.** The micro-Doppler 2D scans from all animals were aligned along the
330 antero-posterior axis with respect to 2 reference cross-sections (B -3.0 and -1.0 mm) selected for their recognizable
331 vascular patterns (Fig. 1c). This alignment for correcting potential shifts occurring either during surgery or imaging.
332 Reference cross-sections were independently identified for every animal by two experts. Any disagreement was
333 resolved post-hoc by consensus. Each micro-Doppler image is then identified by its anatomical position with respect
334 to the Bregma reference point, e.g., B -3.0 mm.

335
336 **Generation of datasets.** Several datasets have been extracted from the initial scans using a down-sampling factor
337 ranging from 2 to 5. This corresponds to an artificial increase in the step size between two consecutive cross-
338 sections. To create the dataset associated with a given factor F, we extracted images from position B -3.0 mm with
339 a step size of $F \times 125 \mu\text{m}$, within the limits of the craniotomy (Fig. 1b). The 5 datasets stepped by [250, 375, 500,
340 625, 750] μm , respectively contain [39, 26, 20, 15, 13] different positions. We randomly selected 50% of the animals
341 for training, 25% for tuning the hyperparameters (validation) and 25% for evaluating the final performances of the
342 model (testing). We augmented the size of the training set with rotations of $\pm 4^\circ$ and $\pm 8^\circ$.

343
344 **Image preprocessing.** To increase the contrast and reduce the intensity amplitude to a [0 1] interval, a correction
345 factor (power of 0.25) has been applied to every pixel of all images in each dataset. The overall process has been
346 implemented using MATLAB (R2018b, Mathworks, USA).

347
348 **Model selection.** To select the best model for the experiments, we evaluated 2 classical CNN architectures
349 (ResNet50⁴¹ and DenseNet121²⁵), SVMs with different feature extraction methods (HOG²⁶, SIFT⁴², PCA) and
350 kernels⁴³. These models were selected for their compatibility with datasets of relatively small sizes. Both ResNet50
351 and DenseNet121 were pretrained on ImageNet⁴⁴ as suggested in ref.⁴⁵. The last layer of the network - the classifier
352 - was replaced by a fully connected layer outputting n values, n being the number of anatomical locations, and
353 passed through a softmax layer afterwards. Both CNN and SVM models were trained and evaluated on the dataset
354 375₂₆, corresponding to the smallest step size above the technology resolution along the antero-posterior axis and
355 therefore the largest dataset without overlapping information. They were respectively implemented with the
356 'torchvision' (PyTorch, version 0.7.0). and 'scikit-learn' (version 0.23.1) Python packages.

357

358 **Training and evaluation procedures for CNNs.** For each of the datasets used in this work, images were resized
359 to 224×320 pixels by bicubic interpolation, and their grey channel extended in RGB to fit the ImageNet format
360 imposed by the pre-training. All the data were normalized with the mean and standard deviation of the full dataset.
361 We augmented the size of the training set with rotations of $\pm 4^\circ$ and $\pm 8^\circ$. The network's weights were optimized with
362 the stochastic gradient descent algorithm using a cross-entropy loss function. The hyperparameters were selected
363 through a random search and the final model performance was evaluated on the testing set. The overall procedure
364 has been performed on a single machine, equipped with Xeon E5-2620 CPU (Intel, USA), 64 Gb RAM and 4
365 RTX2080 (8 GB) GPUs (Nvidia, USA).

366
367 **Visualization of relevant features for image classification using GradCAM.** We extracted the pixels in the input
368 image driving the classification using the Gradient-weighted Class Activation Map (GradCAM) technique, following
369 the recommendations from ref.⁴⁶ on the relevant visualization approaches. Briefly, this method aggregates the
370 gradients associated with the prediction for each feature map in a given layer, to produce a coefficient measuring
371 the contribution of each of the map to the network's prediction. Here, the gradients and feature maps were extracted
372 at the last layer before the classifier. The output heatmaps were then resized by bilinear interpolation to the original
373 image and thresholded at 0.7 to limit the effect of interpolation on the map.

374
375 **GradCAM registration on stereotaxic atlases for anatomical regions extraction.** We used a digital version of
376 the rat Paxinos atlas^{23,30} to extract the anatomical regions associated with the GradCAM. The input scan was taken
377 as a volume and interpolated to fit the atlas resolution (50×50×50 μm^3 voxel size). A 3D rigid registration was
378 performed using a MATLAB custom script^{11,30}. This procedure has been applied to all the samples from the
379 validation and testing sets by an expert. To extract the regions from the GradCAM heatmap, a volume (89 planes
380 as the input data) was constructed from the heatmaps by zero-padding the missing sections before applying the
381 transformation matrix.

382
383 **Evaluation on the stroke dataset.** We used 28 rats subjected to stroke (see above and ref.³⁰). All rats were imaged
384 in the original dataset, and 14/7/7 individuals were respectively present in training/validation/testing sets. The scans
385 were registered and a dataset with 500 μm step size was created following the same procedure as for the previous
386 experiment. The classes predictions were obtained by processing the images through the DenseNet121-CNN and
387 HOG-SVM previously trained on dataset 500₂₀ without re-training.
388

389 **REFERENCES**

- 390 1. Blinder, P. *et al.* The cortical angiome: an interconnected vascular network with
391 noncolumnar patterns of blood flow. *Nat. Neurosci.* **16**, 889–897 (2013).
- 392 2. Kirst, C. *et al.* Mapping the fine-scale organization and plasticity of the brain vasculature.
393 *Cell* **180**, 780-795.e25 (2020).
- 394 3. Todorov, M. I. *et al.* Machine learning analysis of whole mouse brain vasculature. *Nat.*
395 *Methods* **17**, 442–449 (2020).
- 396 4. Attwell, D. *et al.* Glial and neuronal control of brain blood flow. *Nature* **468**, 232–243
397 (2010).
- 398 5. Rungta, R. L., Chaigneau, E., Osmani, B.-F. & Charpak, S. Vascular
399 compartmentalization of functional hyperemia from the synapse to the Pia. *Neuron* **99**,
400 362-375.e4 (2018).
- 401 6. Iadecola, C. The neurovascular unit coming of age: A journey through neurovascular
402 coupling in health and disease. *Neuron* **96**, 17–42 (2017).
- 403 7. Kaplan, L., Chow, B. W. & Gu, C. Neuronal regulation of the blood-brain barrier and
404 neurovascular coupling. *Nat. Rev. Neurosci.* **21**, 416–432 (2020).
- 405 8. Urban, A. *et al.* Understanding the neurovascular unit at multiple scales: Advantages and
406 limitations of multi-photon and functional ultrasound imaging. *Adv. Drug Deliv. Rev.* **119**,
407 73–100 (2017).
- 408 9. Logothetis, N. K. What we can do and what we cannot do with fMRI. *Nature* **453**, 869–878
409 (2008).
- 410 10. Matthews, P. M., Honey, G. D. & Bullmore, E. T. Applications of fMRI in translational
411 medicine and clinical practice. *Nat. Rev. Neurosci.* **7**, 732–744 (2006).
- 412 11. Brunner, C. *et al.* Whole-brain functional ultrasound imaging in awake head-fixed mice.
413 *Nat. Protoc.* **16**, 3547–3571 (2021).
- 414 12. Edelman, B. J. & Macé, E. Functional ultrasound brain imaging: Bridging networks,
415 neurons, and behavior. *Curr. Opin. Biomed. Eng.* **18**, 100286 (2021).
- 416 13. Bercoff, J. *et al.* Ultrafast compound Doppler imaging: providing full blood flow
417 characterization. *IEEE Trans. Ultrason. Ferroelectr. Freq. Control* **58**, 134–147 (2011).
- 418 14. Macé, E. *et al.* Functional ultrasound imaging of the brain. *Nat. Methods* **8**, 662–664
419 (2011).
- 420 15. Mace, E. *et al.* Functional ultrasound imaging of the brain: theory and basic principles.
421 *IEEE Trans. Ultrason. Ferroelectr. Freq. Control* **60**, 492–506 (2013).
- 422 16. Urban, A. *et al.* Chronic assessment of cerebral hemodynamics during rat forepaw
423 electrical stimulation using functional ultrasound imaging. *Neuroimage* **101**, 138–149
424 (2014).
- 425 17. Macé, É. *et al.* Whole-brain functional ultrasound imaging reveals brain modules for
426 visuomotor integration. *Neuron* **100**, 1241-1251.e7 (2018).
- 427 18. Sans-Dublanc, A. *et al.* Optogenetic fUSI for brain-wide mapping of neural activity
428 mediating collicular-dependent behaviors. *Neuron* **109**, 1888-1905.e10 (2021).
- 429 19. Nunez-Elizalde, A. O. *et al.* Neural basis of functional ultrasound signals. *bioRxiv* (2021)
430 doi:10.1101/2021.03.31.437915.
- 431 20. Dizeux, A. *et al.* Functional ultrasound imaging of the brain reveals propagation of task-
432 related brain activity in behaving primates. *Nat. Commun.* **10**, 1400 (2019).
- 433 21. Norman, S. L. *et al.* Single-trial decoding of movement intentions using functional
434 ultrasound neuroimaging. *Neuron* **109**, 1554-1566.e4 (2021).
- 435 22. Wang, Q. *et al.* The Allen mouse brain common coordinate framework: A 3D reference
436 atlas. *Cell* **181**, 936-953.e20 (2020).
- 437 23. Paxinos, G. & Watson, C. *Rat brain in stereotaxic coordinates.* (Academic Press, 2007).
- 438 24. Nouhoum, M. *et al.* A functional ultrasound brain GPS for automatic vascular-based
439 neuronavigation. *Sci. Rep.* **11**, 15197 (2021).

- 440 25. Huang, G., Liu, Z., Van Der Maaten, L. & Weinberger, K. Q. Densely connected
441 convolutional networks. in *2017 IEEE Conference on Computer Vision and Pattern*
442 *Recognition (CVPR)* (IEEE, 2017). doi:10.1109/cvpr.2017.243.
- 443 26. Dalal, N. & Triggs, B. Histograms of oriented gradients for human detection. in *2005 IEEE*
444 *Computer Society Conference on Computer Vision and Pattern Recognition (CVPR'05)*
445 (IEEE, 2005). doi:10.1109/cvpr.2005.177.
- 446 27. Selvaraju, R. R. *et al.* Grad-CAM: Visual explanations from deep networks via gradient-
447 based localization. in *2017 IEEE International Conference on Computer Vision (ICCV)*
448 (IEEE, 2017). doi:10.1109/iccv.2017.74.
- 449 28. Dorr, A., Sled, J. G. & Kabani, N. Three-dimensional cerebral vasculature of the CBA
450 mouse brain: a magnetic resonance imaging and micro computed tomography study.
451 *Neuroimage* **35**, 1409–1423 (2007).
- 452 29. McNEMAR, Q. Note on the sampling error of the difference between correlated
453 proportions or percentages. *Psychometrika* **12**, 153–157 (1947).
- 454 30. Brunner, C. *et al.* Brain-wide continuous functional ultrasound imaging for real-time
455 monitoring of hemodynamics during ischemic stroke. (2022)
456 doi:10.1101/2022.01.19.476904.
- 457 31. Nouhoum, M. *et al.* Fully-automatic ultrasound-based neuro-navigation : The functional
458 ultrasound brain GPS. *Research Square* (2021) doi:10.21203/rs.3.rs-382732/v1.
- 459 32. Rau, R. *et al.* 3D functional ultrasound imaging of pigeons. *Neuroimage* **183**, 469–477
460 (2018).
- 461 33. Demene, C. *et al.* Functional Ultrasound Imaging of the thalamo-cortical auditory tract in
462 awake ferrets using ultrafast Doppler imaging. in *2016 IEEE International Ultrasonics*
463 *Symposium (IUS)* (IEEE, 2016). doi:10.1109/ultsym.2016.7728659.
- 464 34. Brunner, C. *et al.* A platform for brain-wide volumetric functional ultrasound imaging and
465 analysis of circuit dynamics in awake mice. *Neuron* **108**, 861-875.e7 (2020).
- 466 35. Rabut, C. *et al.* 4D functional ultrasound imaging of whole-brain activity in rodents. *Nat.*
467 *Methods* **16**, 994–997 (2019).
- 468 36. Imbault, M. *et al.* Functional ultrasound imaging of the human brain activity: An
469 intraoperative pilot study for cortical functional mapping. in *2016 IEEE International*
470 *Ultrasonics Symposium (IUS)* (IEEE, 2016). doi:10.1109/ultsym.2016.7728505.
- 471 37. Imbault, M., Chauvet, D., Gennisson, J.-L., Capelle, L. & Tanter, M. Intraoperative
472 Functional Ultrasound Imaging of Human Brain Activity. *Sci. Rep.* **7**, 7304 (2017).
- 473 38. Soloukey, S. *et al.* Functional Ultrasound (fUS) During Awake Brain Surgery: The Clinical
474 Potential of Intra-Operative Functional and Vascular Brain Mapping. *Front. Neurosci.* **13**,
475 (2020).
- 476 39. Demene, C. *et al.* Functional ultrasound imaging of the brain activity in human neonates.
477 in *2016 IEEE International Ultrasonics Symposium (IUS)* (IEEE, 2016).
478 doi:10.1109/ultsym.2016.7728657.
- 479 40. Urban, A. *et al.* Functional Ultrasound Imaging of Cerebral Capillaries in Rodents and
480 Humans. *Jacobs Journal of Molecular and Translational Medicine* **1**, (2015).
- 481 41. He, K., Zhang, X., Ren, S. & Sun, J. Deep Residual Learning for Image Recognition. in
482 *2016 IEEE Conference on Computer Vision and Pattern Recognition (CVPR)* 770–778
483 (IEEE, 2016).
- 484 42. Lowe, D. G. Distinctive image features from scale-invariant keypoints. *Int. J. Comput. Vis.*
485 **60**, 91–110 (2004).
- 486 43. Zhang, J., Marszałek, M., Lazebnik, S. & Schmid, C. Local features and kernels for
487 classification of texture and object categories: A comprehensive study. *Int. J. Comput. Vis.*
488 **73**, 213–238 (2007).
- 489 44. Deng, J. *et al.* ImageNet: A large-scale hierarchical image database. in *2009 IEEE*
490 *Conference on Computer Vision and Pattern Recognition* (IEEE, 2009).
491 doi:10.1109/cvpr.2009.5206848.

- 492 45. Tajbakhsh, N. *et al.* Convolutional neural networks for medical image analysis: Full
493 training or fine tuning? *IEEE Trans. Med. Imaging* **35**, 1299–1312 (2016).
494 46. Adebayo, J. *et al.* Sanity Checks for Saliency Maps. *arXiv [cs.CV]* (2018).
495
496

497 **Acknowledgements**

498 This work was supported by grants from the Leducq foundation (Network 15CVD02), from FWO
499 (MEDI-RESCU₂, number AKUL/17/049), from VIB TechWatch (fUSI-MICE) and from internal
500 NERF funding (3D-fUSI project). This research also received funding from the Flemish regional
501 government (AI Research Program). We also thank the NERF animal caretakers including I.
502 Eyckmans, F. Ooms and S. Luijten for their help with management of the rats.

503

504 **Author contributions**

505

	Lambert	Brunner	Kil	Wuyts	D'Hondt	Urban
Concept	X					X
Methodology	X					X
Software						X
Imaging		X				
Data Analysis - Interpretation	X	X	X	X		X
Manuscript	X	X	X	X	X	X
Proof reading	X	X	X	X	X	X
Supervision				X	X	X
Funding					X	X

506

507 **Declaration of interests**

508 A.U. is the founder and a shareholder of AUTC company commercializing functional
509 ultrasound imaging solutions for preclinical and clinical research.